A comparative study of three groups of ductile fracture loci in the 3D space

CrossMark

Yuanli Bai [a,*], Tomasz Wierzbicki [b]

[a] Department of Mechanical and Aerospace Engineering, University of Central Florida, Orlando, FL 32816, United States
[b] Department of Mechanical Engineering, Massachusetts Institute of Technology, Cambridge, MA 02139, United States

A B S T R A C T

Ductile fracture is inherently a three-dimensional phenomenon and should be represented in the 3-D space. Sixteen fracture models are evaluated and divided into three groups: physics based models, phenomenological models and empirical models. These models are then calibrated from the three sets of experimental data, TRIP 690 and TRIP 780 steel sheets and 2024-T351 aluminum alloy. Under the assumption of monotonic loading conditions, major qualitative differences emerged from the comparison of the models in terms of the range of applicability as well as shapes of the 3D fracture envelope are discussed. Several implicit features of these models are revealed.

© 2015 Elsevier Ltd. All rights reserved.

1. Introduction

This paper reports a comparative study on some ductile fracture models in crack-free bodies, which are different from pre-cracked elastic–plastic fracture models based on crack tip mechanics (for examples, [23,33,60]). This topic has become important and gained a lot of attention in recent years since more and more materials with high strength and/or lightweight but less ductility have entered industrial applications. Examples of such materials are advanced high strength steels [1], aluminum alloys, magnesium alloys, polymer matrix composites, and so on. These materials postulate great challenges to the prediction of fracture in manufacturing, forming process, and during service because of less ductility.

Many ductile fracture models have been proposed and extensively investigated in the mechanics community in the past decades. Studies on the micro void based ductile fracture mechanisms are usually attributed to the works by McClintock [53], Rice and Tracey [61]. This part of work had been further carried on by Gurson [26,25] and later Needleman and Tvergaard [57] as a branch of micromechanics. Hancock and Mackenzie [28], Hancock and Brown [27] verified the theories of micro void growth using experiments on notched round bars. Johnson and Cook [34] proposed an empirical model based on these findings and incorporated the effects of strain rate and temperature. Different from Johnson and Cook's model, Wilkins et al. [73] postulated a model with both pressure and stress ratio effects. The effect of stress triaxiality on fracture was put in the framework of continuum damage mechanics by Lemaitre [43] considering the thermodynamics. Instead of using stress triaxiality, Cockcroft and Latham [16] developed a model using the maximum principal stress for predicting cracks during forging of bulk metals, which was further developed by Oh et al. [59].

---

* Corresponding author.
  E-mail addresses: bai@ucf.edu (Y. Bai), wierz@mit.edu (T. Wierzbicki).

Nomenclature

$c_\circ, c_1, c_2, c_3, c_4, \ldots$ coefficients in different fracture models
$\sigma_1, \sigma_2, \sigma_3$ three principal stresses
s_1, s_2, s_3 three principal stresses of deviatoric stress tensor
σ_m mean stress
$\bar{\sigma}$ equivalent stress
σ_Y equivalent stress to yield in Gurson's model
ξ normalized third deviatoric stress invariant
$\bar{\varepsilon}^{pl}$ equivalent plastic strain
$\bar{\varepsilon}_f$ equivalent plastic strain to fracture
D_c critical damage indicator to in different models
A material power strain hardening coefficient, or parameter in Wilkins' fracture model
n material power strain hardening exponent
N number of data points/tests
$c_\theta^{AX}, c_\theta^t, c_\theta^s, c_\theta^c$ parameters in plasticity model by Bai and Wierzibicki
$d_\circ, d_1, d_2, d_3$ different coefficients in Crash-EM fracture model
η stress triaxiality
η_1, η_2 stress triaxiality parameter in Gurson model by Nielsen and Tvergaard
$\eta_{cut-off}$ cut-off value of stress triaxiality below which fracture never occurs
L Lode parameter
χ Lode parameter used in Xue's model
$\bar{\theta}$ Lode angle parameter (normalized Lode angle)
τ_s maximum shear stress to fracture
$\tau_{\max}$ maximum shear stress
k_s fracture model parameter in Crash-FEM model
k_w fracture model parameter in fracture model by Nahshon and Hutchinson
λ fracture parameter in Wilkins' model, or plastic strain amplifier in Gurson's model
μ fracture parameter in Wilkins' model
m fracture parameter in Xue-Wierzbicki's model
f fracture model parameter in Crash-FEM model, or volume fraction of micro void in Gurson type models
$f_\circ, f_f, f_c$ initial or critical volume fractions of micro void in Gurson type models
$\dot{f}_{growth}, \dot{f}_{nucleation}, \dot{f}_{shear}$ changing rate of volume fractions of micro void in Gurson type models
q_1, q_2, s_N, f_N, f^* different coefficients in Gurson type models
ϕ plastic potential function in Gurson type models
F_{zb}^f fracture parameter in McClintock's model

These parts of work were revisited by Bao [7], Bao and Wierzbicki [9] using carefully designed fracture tests together with finite element simulation. Fracture mechanisms of metallic materials were divided into three modes: "ductile fracture", "shear fracture" and mixed mode [9,31]. It was found that the ductile fracture strain is not necessary a monotonic decreasing function of stress triaxiality in general. This finding was further developed by Wierzbicki and Xue [71], Xue [74], Bai and Wierzbicki [5] to incorporate the effect of Lode angle (related to the third deviatroic stress invariant J_3) to ductile fracture. It was shown by Bai and Wierzbicki [6] that these two crack modes and their interaction can be interpreted by the classical Mohr–Coulomb [17,55] fracture model, which considers combined effects of normal stress and shear stress. Experimental results on advanced high strength steels validated the applicability of the modified Mohr–Coulomb model [50,45]. Gao et al. [21] showed strong effects of both pressure and the Lode angle on plasticity and ductile fracture of aluminum 5083 alloy. Lian et al. [46] demonstrated both pressure and Lode angle dependency on ductile fracture of dual-phase steel. Instead of using Lode angle (parameter) but Lode parameter, Lou et al. [48], Lou and Huh [47] proposed a criterion by directly incorporating the existence of cut-off value of stress triaxiality. Khan and Liu [39] proposed an isotropic fracture criterion based on the magnitude of stress vector (MSV), which has been recently extended to study the effect of strain rate and temperature [38]. Voyiadjis et al. [69] studied the ductile fracture use three stress invariants directly and considered the effect of reverse loading.

Introducing the effect of Lode angle was also done for Gurson type micro void based models. Nahshon and Hutchinson [56] and Nielsen and Tvergaard [58] considered the effects of micro void shear by introducing a new term in the evolution equation of micro void volume fraction. Xue [75] took this effect into account by incorporating a shear damage term. Malcher et al. [52] extended the Gurson type model to consider the void shear mechanism and damage effect. Dunand and Mohr [19] compared the prediction of shear modified Gurson models with the modified Mohr–Coulomb model using test data of TRIP-assisted steel sheets. Li et al. [44] evaluated several damage uncoupled/coupled ductile fracture criteria and Gurson–Tvergaard–Needleman (GTN) model using comprehensive test data on Al 6061-T6 alloy. The combining effects of stress

triaxiality and Lode parameter have been studied using unit cell modeling on a representative element from micro mechanics point of view [20,41,15], which provides fundamental understanding of ductile fracture mechanism.

Wierzbicki et al. [72] calibrated and compared seven fracture models in the 2D space of equivalent plastic strain to fracture and the stress triaxiality. Very interesting conclusions were drawn from this study. The ductile fracture strain was shown not to be a monotonic decreasing function of stress triaxiality. However, several hidden or implicit features of those ductile fracture models were not revealed due to the limitation of 2D space. In this paper, a comparison study is made in the 3-D space of the equivalent strain to fracture, stress triaxiality (the normalized hydrostatic pressure) and Lode angle parameter (related to the normalized third deviatoric invariant). Altogether 16 ductile fracture models are divided into three groups: physics based models, phenomenological models and empirical models. Some example models of each group are selected for the comparison study. The physics models include McClintock [53], Rice–Tracey [61], Gurson and GNT models [26,25,57] and shear modified Gurson's model [56,58]. The phenomenological models include maximum shear stress, Cockcroft–Latham [16], pressure modified maximum shear stress, and modified Mohr–Coulomb criterion [6]. The selected empirical models are Johnson–Cook [34], Bao–Wierzbicki [8], Xue–Wierzbicki [72], Wilkins [73], CrashFEM [31,70] and Fracture forming limit diagram (FFLD) [37,22,42]. These models are calibrated from three sets of experimental data on TRIP 690 steel sheet, TRIP780 steel sheet and 2024-T351 aluminum bulk alloy.

It should be noted that there are many other ductile fracture models that are not considered in this paper. Sixteen of them are selected as examples because they are still used in different applications, and are related to the evaluation approach presented here. This paper will give a new method to evaluate and understand different ductile fracture models in terms of their intrinsic features and prediction capabilities under multiaxial stress states, which may be applied to other models as well. Also, the current research is only focused on the fracture loci under assumption of monotonic loading condition. The damage accumulation rules play important roles under nonlinear strain path conditions [3,12], which are not compared in this paper.

2. Transformation equations from principal stresses to two stress state parameters

For isotropic materials, the material properties are independent of the coordinate system rotation, so an arbitrary stress tensor $[\sigma_{ij}]$ can be represented by three principal stresses: σ_1, σ_2 and σ_3. Alternatively, the stress state can be uniquely described by three invariants of the stress tensor, or their ratios as two dimensionless parameters: the stress triaxiality η and Lode angle parameter $\bar{\theta}$, which are defined as follows.
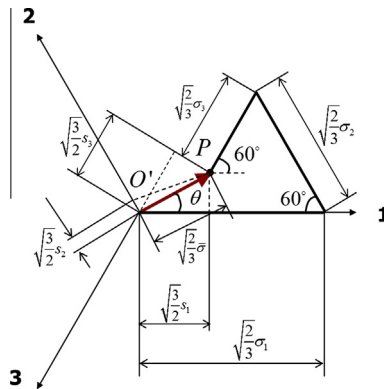
$$\eta = \frac{\sigma_m}{\bar{\sigma}} \tag{1}$$

$$\bar{\theta} = 1 - \frac{6\theta}{\pi} = 1 - \frac{2}{\pi}\arccos\xi \tag{2}$$

where $\sigma_m = (\sigma_1 + \sigma_2 + \sigma_3)/3$ is the mean stress, and σ_1, σ_2 and σ_3 denote three principal stresses. The $\bar{\sigma}$ is the equivalent stress, ξ is defined as normalized third deviatoric stress invariant, $\xi = \frac{27}{2}\frac{J_3}{\bar{\sigma}^3} = \cos(3\theta)$. Here $J_3 = s_1 s_2 s_3$ is the third deviatoric stress invariant. The range of $\bar{\theta}$ is $-1 \leqslant \bar{\theta} \leqslant 1$. Now, all loading conditions can be characterized by the above defined set of parameters $(\eta, \bar{\theta})$. In this paper, ductile fracture models will be reformulated in such a coordinate system.

It was shown by Wierzbicki and Xue [71], Bai and Wierzbicki [5] that the plane stress condition, $\sigma_3 = 0$, uniquely relates the parameters η and ξ or $\bar{\theta}$ through

$$\xi = cos(3\theta) = cos\left[\frac{\pi}{2}(1 - \bar{\theta})\right] = -\frac{27}{2}\eta\left(\eta^2 - \frac{1}{3}\right) \tag{3}$$

Fig. 1. Geometry representation of principal stresses $(\sigma_1, \sigma_2, \sigma_3)$, deviatoric stresses (s_1, s_2, s_3), equivalent stress $(\bar{\sigma})$ and Lode angle (θ) on the deviatoric plane (π plane).

The plane strain condition corresponds to $\bar{\theta} = 0$, while $\bar{\theta} = \pm 1$ are corresponding to axisymmetric tension and axisymmetric compression.

The principal stresses and principal deviatoric stresses can be geometrically represented on the deviatoric plane (π plane), as shown in Fig. 1. Note that all the components are scaled because of the inclined angle between the deviatoric plane and the principal axes. From the geometrical construction, one can easily obtain the expressions of the deviatoric principal stresses in terms of $\bar{\sigma}$ and θ,

$$\begin{cases} \sqrt{\frac{3}{2}} s_1 = \sqrt{\frac{2}{3}} \bar{\sigma} \cos \theta \\ \sqrt{\frac{3}{2}} s_2 = \sqrt{\frac{2}{3}} \bar{\sigma} \cos \left(\frac{2}{3} \pi - \theta \right) \\ \sqrt{\frac{3}{2}} s_3 = \sqrt{\frac{2}{3}} \bar{\sigma} \cos \left(\frac{4}{3} \pi - \theta \right) \end{cases} \Rightarrow \begin{cases} s_1 = \frac{2}{3} \bar{\sigma} \cos \theta \\ s_2 = \frac{2}{3} \bar{\sigma} \cos \left(\frac{2}{3} \pi - \theta \right) \\ s_3 = \frac{2}{3} \bar{\sigma} \cos \left(\frac{4}{3} \pi - \theta \right) \end{cases} \tag{4}$$

Using Eq. (4), one can express the three principal stresses in terms of σ_m, η and θ.

$$\begin{cases} \sigma_1 = \sigma_m + s_1 = \sigma_m + \frac{2}{3} \bar{\sigma} \cos \theta = \left[1 + \frac{2 \cos \theta}{3 \eta} \right] \sigma_m \\ \sigma_2 = \sigma_m + s_2 = \sigma_m + \frac{2}{3} \bar{\sigma} \cos \left(\frac{2}{3} \pi - \theta \right) = \left[1 + \frac{2 \cos \left(\frac{2}{3} \pi - \theta \right)}{3 \eta} \right] \sigma_m \\ \sigma_3 = \sigma_m + s_3 = \sigma_m + \frac{2}{3} \bar{\sigma} \cos \left(\frac{4}{3} \pi - \theta \right) = \left[1 + \frac{2 \cos \left(\frac{4}{3} \pi - \theta \right)}{3 \eta} \right] \sigma_m \end{cases} \tag{5}$$

3. Representation of fracture models in the 3D space of invariants, $\hat{\varepsilon}_f(\eta, \bar{\theta})$

3.1. Physics based models

The first group of ductile fracture models are called physics based models. Six often cited models are selected here: McClintock [53], Rice–Tracey [61], Gurson and GNT models [26,25,57] and shear modified Gurson's models [56,58].

3.1.1. McClintock model (McCl)

In the range of high stress triaxiality, the mechanism of ductile fracture is commonly believed to be governed by micro void growth, nucleation, coalescence, and linkage [53,61]. McClintock analyzed the growth and linkage of two cylindrical voids and concluded that stress triaxiality is the key parameter controlling ductile fracture [53]. An approximate fracture criterion was proposed with a closed-form solution of damage evolution (Eq. (6)) [53].

$$\frac{dD}{d\bar{\varepsilon}} = \frac{1}{\ln F_{zb}^f} \left[\frac{\sqrt{3}}{2(1-n)} \sinh \left(\frac{\sqrt{3}(1-n)}{2} \frac{\sigma_a + \sigma_b}{\bar{\sigma}} \right) + \frac{3}{4} \frac{\sigma_a - \sigma_b}{\bar{\sigma}} \right] \tag{6}$$

where σ_a and σ_b are two principal stresses, F_{zb}^f is the relative void growth factor to fracture, and D is the damage indicator. The symbol n denotes the material power hardening exponent. If we assume that $\sigma_a = \sigma_1 \geqslant \sigma_b = \sigma_2$, which is considered as the worst condition, and fracture occurs at $D = D_c$, then assume proportional loading and use transformation equations (Eq. (5)), we can get the following fracture locus for McClintock's model.

$$\bar{\varepsilon}_f = \frac{\frac{2}{\sqrt{3}}(1-n)D_c}{\sinh \left\{ \sqrt{3}(1-n) \left[\eta - \frac{1}{3} \cos \left(\frac{\pi}{6} (\bar{\theta} + 7) \right) \right] \right\} + (1-n) \sin \left(\frac{\pi}{6} (\bar{\theta} + 1) \right)} \tag{7}$$
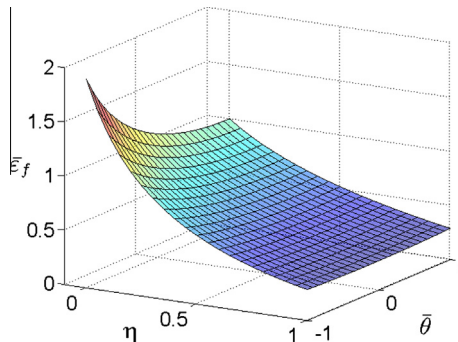

Fig. 2. An example plot of McClintock's fracture locus in the 3D space of $\hat{\varepsilon}_f(\eta, \bar{\theta})$. Take $D_c = 1.0$ and $n = 0.16$ in Eq. (7).

There is only one fracture parameter D_c in Eq. (7) needed to calibrate. A example plot of the McClintock's model is shown in Fig. 2. It is noted that the minimal stress component σ_3 is neglected in the above derivation, but it is taken into account by the overall stress triaxiality brought from Eq. (5). The other case of $\sigma_a = \sigma_1 \geqslant \sigma_2 \geqslant \sigma_b = \sigma_3$ will give the similar result.

One can see that the McClintock's model predicts an asymmetric fracture locus with respect to the Lode angle parameter $\bar{\theta}$. The model predicts week dependency on Lode angle parameter in high stress triaxiality region but strong Lode effect in low stress triaxiality region. It is interesting that the plastic hardening parameter (n) is introduced explicitly into the fracture model.

3.1.2. Rice–Tracey (R–T)

Rice and Tracey [61] studied the growth of spherical void under hydrostatic tensile pressure. The commonly used Rice–Tracey model reads

$$\hat{\varepsilon}_f(\eta, \bar{\theta}) = c_1 \exp(-c_2 \eta) \tag{8}$$

where c_1 and c_2 are two coefficients of the exponential function to calibrate. It was found that the constant c_2 is about 1.5 for many engineering materials. The exponential function derived by Rice and Tracey has been adopted by several empirical fracture models, which will be discussed in Section 3.3.

3.1.3. Gurson, GNT and Shear-modified GNT models (GUR, GNT, GNH, N–T)

Gurson proposed a constitutive model for porous materials with micro voids [26,25]. Needleman and Tvergaard [57] extended the original Gurson's model to consider the void nucleation effect in addition to the void growth mechanism, which is often referred to as GNT model. The Gurson type model defines the following plastic flow potential.

$$\phi = \left(\frac{\bar{\sigma}}{\sigma_Y}\right)^2 + 2q_1 f^* \cos h\left(\frac{3q_2 \sigma_m}{2\sigma_Y}\right) - 1 - (q_1 f^*)^2 = 0 \tag{9}$$

where the f^* reads

$$f^* = \begin{cases} f & \text{for } f \leqslant f_c \\ f_c + \frac{1/q_1 - f_c}{f_f - f_c}(f - f_c) & \text{for } f > f_c \end{cases} \tag{10}$$

In Eqs. (9) and (10), σ_Y is the matrix yield stress, and σ_m is the mean stress, and q_1, q_2 are two parameters in the plastic flow potential. f_c is the critical value of void volume fraction at which material stress carrying capacity starts to decay more rapidly, and f_f corresponds to complete loss of stress-carrying capacity or material fracture. Assuming the associated plastic flow rule, one can derive the increments of plastic strain components as follows.

$$\dot{\varepsilon}_{ij}^{pl} = \Lambda \frac{\partial \phi}{\partial \sigma_{ij}} = \dot{\lambda}\left(\frac{\sigma_Y}{2}\right)\frac{\partial \phi}{\partial \sigma_{ij}} = \dot{\lambda}\left[\frac{3s_{ij}}{2\sigma_Y} + \frac{f^* q_1 q_2}{2} \sinh\left(\frac{3q_2 \sigma_m}{2\sigma_Y}\right)\delta_{ij}\right] \tag{11}$$

where $\dot{\lambda}$ is the equivalent plastic strain rate, $\dot{\lambda} = \dot{\varepsilon}^{pl}$. From Eq. (11), the plastic volumetric strain is an important variable that can be derived as,

$$\dot{\varepsilon}_{kk}^{pl} = \frac{3f^* q_1 q_2}{2} \sinh\left(\frac{3q_2 \sigma_m}{2\sigma_Y}\right)\dot{\lambda} = \frac{3f^* q_1 q_2}{2} \sinh\left(\frac{3}{2}q_2 \eta\right)\dot{\varepsilon}^{pl} \tag{12}$$

The symbol f denotes the volume fraction of micro voids in Gurson type models. When the f increases from an initial value $f_\circ$ to a critical value f_f, then the material point is assumed to fail. The original Gurson's model contain only one failure mechanism called the void growth with the plastic volumetric change.

$$\dot{f}_{growth} = (1 - f)\dot{\varepsilon}_{kk}^{pl} = (1 - f)\frac{3f^* q_1 q_2}{2} \sinh\left(\frac{3q_2 \sigma_m}{2\sigma_Y}\right)\dot{\lambda} = (1 - f)\frac{3f^* q_1 q_2}{2} \sinh\left(\frac{3}{2}q_2 \eta\right)\dot{\varepsilon}^{pl} \tag{13}$$

From Eq. (13), we can see that the material will not fail under compressive loading conditions according to Gurson's model, since the volumetric strain increment ($\dot{\varepsilon}_{kk}^{pl}$) is negative in compression. Needleman and Tvergaard [57] introduced another failure mechanism called the micro voids nucleation due to plastic deformation.

$$\dot{f}_{nucleation} = \frac{f_N}{s_N \sqrt{2\pi}} \exp\left[-\frac{1}{2}\left(\frac{\varepsilon^{pl} - \varepsilon_N}{s_N}\right)^2\right]\dot{\varepsilon}^{pl} \tag{14}$$

where f_N is the volume fraction of void nucleating particles. ε_N and s_N are the mean strain and standard deviation for nucleation respectively. Nahshon and Hutchinson [56] noticed the limitation of original Gurson's model, which considers only the effect of stress triaxiality. They introduced another failure mechanism to describe the micro voids shear localization, which is called "void shear" here.

$$\dot{f}_{shear} = k_w f(1 - \xi^2)\frac{s_{ij}\dot{\varepsilon}_{ij}^{pl}}{\bar{\sigma}} = k_w f(1 - \xi^2)\frac{\bar{\sigma}}{\sigma_Y}\dot{\lambda} = k_w f(1 - \xi^2)\dot{\varepsilon}^{pl} \tag{15}$$

where ξ is the normalized third deviatoric stress invariant, and k_w is a new material coefficient. Recently, Nielsen and Tvergaard [58] modified the shear effect term to make it focused on negative and low stress triaxiality region. The additional constrain term $\Omega(\eta)$ reads,

$$\Omega(\eta) = \begin{cases} 1 & \eta < \eta_1 \\ (\eta - \eta_2)/(\eta_1 - \eta_2) & \eta_1 \leqslant \eta < \eta_2 \\ 0 & \eta > \eta_2 \end{cases} \tag{16}$$

Assuming all three micro mechanisms are independent, the total governing equation of micro voids fraction is,

$$\dot{f} = \dot{f}_{growth} + \dot{f}_{nucleation} + \dot{f}_{shear}$$
$$= \left\{ (1-f)\frac{3f^* q_1 q_2}{2} \sinh\left(\frac{3}{2}q_2\eta\right) + \frac{f_N}{s_N\sqrt{2\pi}} \exp\left[-\frac{1}{2}\left(\frac{\varepsilon^{pl} - \varepsilon_N}{s_N}\right)^2\right] + k_w f (1 - \xi^2)\Omega(\eta) \right\} \dot{\varepsilon}^{pl} \tag{17}$$

The initial boundary conditions for this differential equation are $f = f_\circ$ and $\varepsilon^{pl} = 0$. Material points are assumed to fail when $f = f_f$. The Gurson type of fracture models are physics based, and found a lot of applications since they were developed. A summary of the evolution equations of micro void fraction for different version of Gurson type fracture model is listed in Table 1.

In order to visualize these fracture models, one needs to convert these models to the three-dimensional space of stress triaxiality η, Lode angle parameter $\bar{\theta}$ and equivalent strain to fracture $\bar{\varepsilon}_f$. For proportional loading conditions, the stress triaxiality η becomes a constant. The normalized third deviatoric stress invariant ξ, which can be related to the Lode angle parameter $\bar{\theta}$ by Eq. (3), is also constant. Hence, the differential equations listed in Table 1 can be solved using numerical integration. A Matlab code is written to do the integration. It is also noted that closed form solutions can be derived for the original Gurson's model (Eq. (18)) and Nahshon-Hutchinson's model (Eq. (19)).

$$\hat{\varepsilon}_f(\eta, \bar{\theta}) = \frac{1}{k_1} \ln\left[\frac{f_f(1 - f_\circ)}{f_\circ(1 - f_f)}\right] \tag{18}$$

$$\hat{\varepsilon}_f(\eta, \bar{\theta}) = \frac{1}{k_1 + k_2} \ln\left[\frac{f_f(-k_1 f_\circ + k_1 + k_2)}{f_\circ(-k_1 f_f + k_1 + k_2)}\right] \tag{19}$$

where $k_1 = \frac{3q_1 q_2}{2} \sinh\left(\frac{3}{2}q_2\eta\right)$ and $k_2 = k_w(1 - \xi^2) = k_w\{1 - \cos^2\left[\frac{\pi}{2}(1 - \bar{\theta})\right]\}$. Three dimensional plots of fracture loci for these models are shown in the following model calibration sections.

3.2. Phenomenological models

The second group of ductile fracture models are called phenomenological models. Four typical models chosen for comparison are: maximum shear stress model [17,67], Cockcroft–Latham [16], pressure modified maximum shear stress, and modified Mohr–Coulomb (MMC) criterion [6]. Recently, [19] demonstrated that the MMC model captures shear localization, which is the main fracture mode for low and negative stress triaxiality regions.

3.2.1. Maximum shear stress (MSS)

One of the oldest failure model is the maximum shear stress model by Coulomb [17] and Tresca [67], which is still used for many civil engineering materials. This model assumes fracture will occurs when the maximum shear stress reaches a critical value τ_s on one of the shear planes.

$$\tau^f_{max} = \tau_s \tag{20}$$

If the J2 material plasticity and the power hardening law are assumed, then one can get the following fracture locus [6].

$$\hat{\varepsilon}_f(\eta, \bar{\theta}) = \left\{\frac{\sqrt{3}}{3} \frac{A}{\tau_s} \cos\left(\frac{\bar{\theta}\pi}{6}\right)\right\}^{-\frac{1}{n}} \tag{21}$$

Table 1
Summary of different models of Gurson type.[a]

Models	Evolution equations of f
Gurson [25]	$\dot{f} = (1 - f)\frac{3q_1 q_2}{2} \sinh\left(\frac{3}{2}q_2\eta\right)\dot{\varepsilon}^{pl}$
GNT [68]	$\dot{f} = \left\{(1 - f)\frac{3f^* q_1 q_2}{2} \sinh\left(\frac{3}{2}q_2\eta\right) + \frac{f_N}{s_N\sqrt{2\pi}} \exp\left[-\frac{1}{2}\left(\frac{\varepsilon^{pl} - \varepsilon_N}{s_N}\right)^2\right]\right\}\dot{\varepsilon}^{pl}$
GNH [56]	$\dot{f} = \left[(1 - f)\frac{3f q_1 q_2}{2} \sinh\left(\frac{3}{2}q_2\eta\right) + k_w f\left(1 - \xi^2\right)\right]\dot{\varepsilon}^{pl}$
N–T [58]	Eq. (17)

[a] The boundary conditions are $f = f_\circ$ at $\varepsilon^{pl} = 0$, and $f = f_f$ at $\varepsilon^{pl} = \bar{\varepsilon}_f$.

where A and n are two plastic power hardening constants ($\bar{\sigma} = A\bar{\varepsilon}^n$). There is only one fracture parameter in this model, τ_s.

3.2.2. Cockcroft–Latham (C–L)

Cockcroft and Latham [16] proposed a ductile fracture model in which the increment of the damage parameter was $dD = \langle \sigma_1 \rangle d\bar{\varepsilon}^{pl}$. The integral form of this equation is

$$\int_0^{\bar{\varepsilon}_f} \langle \sigma_1 \rangle d\bar{\varepsilon}^{pl} = D_c \tag{22}$$

Here σ_1 is the maximum principal tensile stress. The symbol $\langle \sigma_1 \rangle$ is the Macauley bracket, which renders the value of σ_1 if σ_1 is positive and zero if all the principal stresses are negative. The integral of C–L model indicates the physical dimension of energy density. Oh et al. [59] modified the C–L model by introducing the normalized maximum principal stress $\frac{\sigma_1}{\bar{\sigma}}$ as the weighting function.

$$\int_0^{\bar{\varepsilon}_f} \frac{\langle \sigma_1 \rangle}{\bar{\sigma}} d\bar{\varepsilon}^{pl} = D_c \tag{23}$$

This model is referred as Cockcroft–Latham model in the paper as well. Under proportional loading conditions, the weighting function in the integral Eq. (23) is a constant, so the fracture strains under different loading conditions can be explicitly derived. Furthermore, the value of σ_1 could be substituted by Eq. (5). The resulted fracture locus becomes,

$$\bar{\varepsilon}_f(\eta, \bar{\theta}) = \frac{D_c \bar{\sigma}}{\sigma_1} = \frac{3D_c}{3\eta + 2\cos\left(\frac{\pi}{6}(1 - \bar{\theta})\right)} \tag{24}$$

There is only one fracture parameter D_c needed to be calibrated. The Eq. (24) imply a cut-off region where fracture strains become infinity.

$$3\eta + 2\cos\left(\frac{\pi}{6}(1 - \bar{\theta})\right) \leqslant 0 \tag{25}$$

For axial symmetric compression, $\bar{\theta} = -1$, the cutoff value is $\eta_{cutoff} = -1/3$. For plane strain condition, $\bar{\theta} = 0$, the cutoff value is $\eta_{cutoff} = -\sqrt{3}/3$. For axial symmetric tension, $\bar{\theta} = 1$, the cutoff value is $\eta_{cutoff} = -2/3$.

The Cockcroft–Latham fracture model was originally developed for bulk metal forming such as forging. Tarigopula et al. [64] demonstrated its applicability to sheet metal forming processes. More recently, it was also used with success in problems involving high velocity penetration and perforation of metal plates [13]. It is noted that the implicitly built-in cut-off fracture region makes the Cockcroft–Latham model applicable for high velocity impact simulation.

3.2.3. Modified Mohr–Coulomb criterion (MMC)

Mohr–Coulomb criterion [17,55] has been widely used in describing plasticity and fracture of brittle geomaterials. This model postulate the following fracture criterion.

$$max(\tau + c_1 \sigma_n)_f = c_2 \tag{26}$$

where τ and σ_n are shear and the normal stress on the fracture plane. The c_1 and c_2 are two material constants. Bai and Wierzbicki [6] extended the applicability of Mohr–Coulomb criterion to ductile fracture, and proposed the Modified Mohr–Coulomb (MMC) fracture model. The MMC fracture locus reads

$$\bar{\varepsilon}_f = \left\{ \frac{A}{c_2} \left[c_\theta^s + \frac{\sqrt{3}}{2 - \sqrt{3}} (c_\theta^{AX} - c_\theta^s) \left(\sec\left(\frac{\bar{\theta}\pi}{6}\right) - 1 \right) \right] \left[\frac{\sqrt{3}}{3} \cos\left(\frac{\bar{\theta}\pi}{6}\right) + c_1 \left(\eta + \frac{1}{3} \sin\left(\frac{\bar{\theta}\pi}{6}\right) \right) \right] \right\}^{-\frac{1}{n}} \tag{27}$$

where A and n are two power hardening coefficients, and c_1, c_2 and c_θ^s are three fracture parameters. The c_θ^{AX} is defined as Eq. (28). The c_θ^t is usually set as unity, and c_θ^c is the fourth parameter considering the asymmetry of a fracture locus. If one takes $c_\theta^c = 1$ for simplicity, then $c_\theta^{AX} = 1$ in Eq. (27). This kind of MMC fracture locus has only three fracture parameters (c_1, c_2 and c_θ^s), which is referred as MMC3. Otherwise, there will be four parameters (c_1, c_2, c_θ^s and c_θ^c), which is called MMC4. In the present paper, the MMC3 is used and referred as MMC hereafter by default.

$$c_\theta^{AX} = \begin{cases} c_\theta^t = 1.0 & for \quad \bar{\theta} \geqslant 0 \\ c_\theta^c & for \quad \bar{\theta} < 0 \end{cases} \tag{28}$$

The MMC model implies a cutoff region for the fracture locus.

$$\sqrt{\frac{1 + c_1^2}{3}} \cos\left(\frac{\bar{\theta}\pi}{6}\right) + c_1 \left(\eta + \frac{1}{3} \sin\left(\frac{\bar{\theta}\pi}{6}\right) \right) \leqslant 0 \tag{29}$$

This cutoff region depends only on the "friction" parameter c_1. The physical explanation of MMC model's cutoff region is the existing of "die cone" in friction analysis.

Note that this model has been extended to capture anisotropic fracture by Luo et al. [51]. Another evolution of this model [54] is to replace or link the parameter of c_θ^s with the power coefficient m in Hosford non-quadratic yield function [32], which is called extended Mohr–Coulomb (EMC) model. The EMC is a simplified version of MMC, which is similar to MMC3 (constraining same fracture strains under axial symmetric compression and axial symmetric tension). These two features will not be discussed in the paper.

3.2.4. Pressure modified maximum shear stress (PMMS)

A natural modification of the maximum shear stress criterion is the pressure modified maximum shear stress criterion (PMMS), which considers the hydrostatic pressure effect on ductile fracture.

$$(\tau_{max} + c_1 \sigma_m)_f = c_2 \tag{30}$$

where σ_m is the mean stress at the maximum shear stress plane. The c_1 and c_2 are two material constants. The maximum shear stress is half of the difference between maximum and minimum principal stresses, $\tau_{max} = \frac{1}{2}(\sigma_1 - \sigma_3)$ for $\sigma_1 \geqslant \sigma_2 \geqslant \sigma_3$. Substituting Eq. (5) into Eq. (30), one can convert the fracture model from the stress space to the strain space using the material hardening law. The following fracture locus is derived. The detail derivation steps are similar to the modified Mohr–Coulomb model shown in Ref. [6].

$$\bar{\varepsilon}_f = \left\{ \frac{A}{c_2} \left[c_\theta^s + \frac{\sqrt{3}}{2 - \sqrt{3}} \left(c_\theta^{AX} - c_\theta^s \right) \left(\sec \left(\frac{\bar{\theta}\pi}{6} \right) - 1 \right) \right] \left[\frac{\sqrt{3}}{3} \cos \left(\frac{\bar{\theta}\pi}{6} \right) + c_1 \eta \right] \right\}^{-\frac{1}{n}} \tag{31}$$

The fracture parameters in Eq. (31) are similar to the MMC model. There is also a cutoff region in the PMMS fracture locus, which reads

$$\frac{\sqrt{3}}{3} \cos \left(\frac{\bar{\theta}\pi}{6} \right) + c_1 \eta \leqslant 0 \tag{32}$$

For plane strain condition, $\bar{\theta} = 0$, the cutoff value is $\eta_{cutoff} = -\frac{\sqrt{3}}{3c_1}$. This cutoff region is dependent only on parameter c_1.

3.3. Empirical models

The third group of ductile fracture models are empirical models. Five typical models are selected for comparison: Johnson–Cook model [34], Bao–Wierzbicki [8], Xue–Wierzbicki [72], CrashFEM [30,70], and fracture forming limit diagram (FFLD).

3.3.1. Johnson–Cook (J–C)

Johnson–Cook's fracture model [34] is one of the models that are widely used. A part of its popularity is that Johnson and Holmquist [35] gave a list of material plasticity and fracture data for many structural materials. The J–C model considers not only the effect of stress triaxiality, but also the strain rate and temperature dependency. In this paper, we consider only the stress state effects. The stress triaxiality function in J–C model adopts the exponential function as the Rice–Tracey model by adding one constant parameter $c_\circ$.

$$\hat{\varepsilon}_f(\eta, \bar{\theta}) = c_\circ + c_1 \exp(-c_2 \eta) \tag{33}$$

where $c_\circ, c_1$ and c_2 are three parameters in the exponential function. There is no cutoff value in the J–C model. In this comparison study, we combine Johnson–Cook and Rice–Tracey together, and only the J–C model is evaluated since these two models are very similar.

Note that the recent work by Beissel et al. [11] extended the Johnson–Cook's model to consider the effect of the third deviatoric stress invariant, which describes the strength difference between triaxial extension and triaxial compression. The form of Lode angle dependency by Gudehus [24] was adopted. The new version of Johnson–Cook's model is not evaluated in this paper.

3.3.2. Bao–Wierzbicki (B–W) and Xue–Wierzbicki (X–W)

Bao and Wierzbikci conducted a series of experiments and found that the ductile fracture strain is not necessarily a monotonic function of the stress triaxiality [7,8]. A three-branch empirical fracture locus in the space of stress triaxiality and equivalent plastic strain to fracture was proposed. In the high triaxiality region, the B–W model takes the same exponential function as J–C or R–T model because the dominant failure mechanism is void growth and linkage. In the negative stress triaxiality region, it was found to be shear fracture dominated. In the low stress triaxiality region, a cutoff value of $\eta = -1/3$ was postulated [10] based on a careful revisit of Bridgman's test data [14]. This model is independent of the Lode angle effect.

It should be noted that the B–W model was based on a careful examination of 15 types of specimens, each developing a different history of triaxiality. Most but not all specimens were in the plane stress state. Therefore, the effect of Lode angle was not included in the analysis. The B–W model is thus of more historical value. It is one of the most cited papers in the

recent literature on ductile fracture because it revealed for the first time the non-monotonic dependence of fracture strains on stress triaxiality.

A successor of the B–W model is the pure empirical Xue–Wierzibicki (X–W) model [72] after introducing the effect of the third deviatoric stress invariant J_3, which is related to the Lode angle parameter $\bar{\theta}$ (see Eq. (2)). The model reads,

$$\hat{\varepsilon}_f(\eta, \xi) = c_1 \exp(-c_2\eta) - [c_1 \exp(-c_2\eta) - c_3 \exp(-c_4\eta)](1 - \xi^m)^{1/m} \tag{34}$$

where $c1, c2, c3, c4$ are four material constants, and m is an even integer. This model takes the exponential function of J–C or R–T model to describe the lower bound (plane strain condition, $c_3 \exp(-c_4\eta)$) and the upper bound (axial symmetric condition, $c_1 \exp(-c_2\eta)$) of a 3D fracture locus. A symmetric non-quadratic elliptic function is assumed to describe the effect of J_3 between two bound limits.

3.3.3. Wilkins model (WKS)

This is a model which was developed more than thirty years ago by Wilkins et al. [73]. It considers the effects of mean stress(pressure), deviatoric stress ratio, and length scale effect on the ductile fracture. The model has been further renewed and developed into PAM-CRASH FE code [36], and referred as extended Wilkins-Kamoulakos (EWK) fracture model. The Wilkins model postulated that fracture occurs when the following integral exceeds a critical value D_c over a critical dimension R_c.

$$D_c = \int_0^{\bar{\varepsilon}_f} \frac{1}{(1 - a\sigma_m)^\lambda}(2 - A)^\mu d\bar{\varepsilon}^{pl} \tag{35}$$

where,

$$A = \max\left(\frac{s_2}{s_1}, \frac{s_2}{s_3}\right) \tag{36}$$

In this definition, s_1, s_2, s_3 are three deviatoric principal stresses ($s_1 \geqslant s_2 \geqslant s_3$). a is the coefficient for mean stress effect. λ and μ are two coefficients in the corresponding power functions. D_c and R_c will be determined by suitable designed calibration procedure. The dimension parameter R_c will play an important role where there is large strain gradient at fracture sites, but this effect will not be evaluated in this paper. Using the similar approach under proportional loading assumption, the fracture locus of Wilkins model can be expressed as the following way,

$$\bar{\varepsilon}_f = D_c(1 - a\sigma_m)^\lambda(2 - A)^{-\mu} = D_c(1 - a\bar{\sigma}\eta)^\lambda(2 - A)^{-\mu} \tag{37}$$

The mean stress σ_m is replaced by $\bar{\sigma}\eta$. It is further assumed that $a\bar{\sigma}$ can be simplified as a constant (c_1) during plastic deformation if the material strain hardening is not significant. From the definition of parameter A, we can substitute Eq. (4) into Eq. (36). Note that $s_1 \geqslant s_2 \geqslant s_3$ is automatically satisfied for the Lode angle within $0 \leqslant \theta \leqslant \pi/3$. The transformation of A to $\bar{\theta}$ is shown in Eq. (38). The result can be further simplified as $A \approx |\bar{\theta}|$ if needed.

$$A = \max\left(\frac{s_2}{s_1}, \frac{s_2}{s_3}\right) = \begin{cases} \frac{s_2}{s_3} & \text{if} \quad 0 \leqslant \theta \leqslant \frac{\pi}{6} \\ \frac{s_2}{s_1} & \text{if} \quad \frac{\pi}{6} \leqslant \theta \leqslant \frac{\pi}{3} \end{cases} = \frac{\sin\left(|\bar{\theta}|\pi/6\right)}{\cos\left[(1 + |\bar{\theta}|)\pi/6\right]} \tag{38}$$

Finally, the following approximated 3D fracture locus for Wilkins model is obtained for the comparison study.

$$\bar{\varepsilon}_f(\eta, \bar{\theta}) \approx D_c(1 - c_1\eta)^\lambda \left[2 - \frac{\sin\left(|\bar{\theta}|\pi/6\right)}{\cos\left((1 + |\bar{\theta}|)\pi/6\right)}\right]^{-\mu} \tag{39}$$

where D_c, c_1, λ, μ are four free material parameters. It is noted that the Wilkins fracture locus is a symmetric function of $\bar{\theta}$, which does not distinguish axial symmetric tension and axial symmetric compression. There is no cutoff value in Wilkins model.

3.3.4. CrashFEM Fracture Model (C-F)

The BMW R&D Center and MATFEM Co. in Munich proposed a comprehensive fracture model [30,70], which includes three failure mechanisms: instability, ductile fracture and shear fracture. If any one of the criteria is met, then a material element is assumed to fail. The model is referred as CrashFEM (C-F) in this paper. This model is mainly applicable to thin sheets and extrusions (plane stress condition). In order to overcome the mesh size dependency and make the model suitable for metal sheets application, the modified forming limit diagram (FLD) was included in the C-F model. In the modified FLD, the necking is described by equivalent strain to neck and strain ratio [70]. The second mechanism is the ductile fracture due to void growth. The equivalent strain to fracture is assumed to be a function of stress triaxiality.

$$\hat{\varepsilon}_{f,ductile}(\eta, \bar{\theta}) = d_\circ \exp(-3c\eta) + d_1 \exp(3c\eta) \tag{40}$$

where $c, d_\circ$ and d_1 are three material constants. In the shear fracture dominated zone(the third mechanism), the following fracture locus is postulated.

$$\hat{\varepsilon}_{f,shear}(\eta, \bar{\theta}) = d_2 \exp\{-f\theta_s\} + d_3 \exp\{f\theta_s\} \tag{41}$$

The new "shear fracture" parameter θ_s is defined by

$$\theta_s = \frac{\bar{\sigma}}{\tau_{\max}}(1 - 3k_s\eta) = \frac{\sqrt{3}}{\sin\left[\frac{\pi}{6}(3 + \bar{\theta})\right]}(1 - 3k_s\eta) \tag{42}$$

where f, d_2, d_3 and k_s are additional four material constants. Using the transformation equations for maximum shear stress τ_{max}, one can express the parameter θ_s in terms of stress triaxiality and Lode angle parameter, which is shown in the second part of Eq. (42). Substituting Eq. (42) into Eq. (41), one can get the shear fracture locus of C-F model.

$$\hat{\varepsilon}_{f,shear}(\eta, \bar{\theta}) = d_2 \exp\left\{-f\frac{\sqrt{3}}{\sin\left[\frac{\pi}{6}(3 + \bar{\theta})\right]}(1 - 3k_s\eta)\right\} + d_3 \exp\left\{f\frac{\sqrt{3}}{\sin\left[\frac{\pi}{6}(3 + \bar{\theta})\right]}(1 - 3k_s\eta)\right\} \tag{43}$$

Note that the FLD is a necking criterion rather than fracture criterion. One consideration to be included into the C–F model is to solve mesh size sensitivity in shell elements. In the comparison study of this paper, emphasis will be put in the ductile and shear fracture mechanism. Also, there is a new evolution of this model to consider nonlinear strain path [29], which will not be discussed in this paper.

3.3.5. Fracture Forming Limit Diagram (FFLD)

The FFLD [40,2] has been used in the metal forming industry to describe transition from plane stress necking to transverse plane strain fracture. Lee [42] collected many experimental data on metal sheets and used the following approximation formulation.

$$\varepsilon_{1f} + \varepsilon_{2f} = -\varepsilon_{3f} = c \tag{44}$$

where c is the only material constant. Note that the fracture locus in the space of two in-plane principal strains can be a general curve (not necessarily a straight line). The line equation (Eq. (44)) is only the first order approximation. It should be noted that the FFLD can only be used for plane stress condition.

If one likes to convert the all strain based FFLD (Eq. (44)) to the mixed strain and stress invariants 3D space used in the present paper, a curtain plastic flow rule should be assumed to link the strain ratio to stress ratio. Such a procedure can be found in Ref [4]. On the contrary, ductile fracture models can also be converted to the FFLD space for comparison, which will be summarized in Section 6.2.

4. Model calibrations for bulk 2024-T351 aluminum alloy

The first example used in the comparison study is the test data of 2024-T351 aluminum alloy reported by Bao and Wierzbicki [8,72]. Fifteen different types of specimen were used to calibrate the equivalent strains to fracture of this material for a wide range of stress states. A summary of test results can be found in Table 1 of Ref. [6]. These data were also revisited by Stoughton and Yoon [63] and Khan and Liu [39]. Those tests were conducted under monotonic loading conditions, but there were some changes of stress state parameters (η and $\bar{\theta}$) as loading increases and deformation continues. Since the damage evolution rule is not the focus of this paper, the average values of η and $\bar{\theta}$ are used, which is also consistent with the definition of fracture locus (under proportional loading conditions).

Optimization using a Matlab code are conducted here to identify parameters of the above fracture models. The following optimization objective function, Eq. (45), are used, where N is the number of fracture tests, $\bar{\varepsilon}_{f,i}$ denotes fracture strain from test, and $\hat{\varepsilon}_f(\eta_i, \bar{\theta}_i)$ is fracture strain from model prediction. A list of calibrated model parameters are summarized in the Table 2. The parameters determined from tests directly are put in (*) of the table, which are not included in the optimization

Table 2
A list of calibrated model parameters for 2024-T351 aluminum alloy.

Model	Parameters[a]	Average error
McCl	$D_c = 0.5316, (n = 0.153)$	43.37%
J–C	$c_o = 0, c_1 = 0.3208, c_2 = 0.7028$	21.90%
B–W	As indicated in Eq. (4) of Ref. [66]	N/A
X–W	$c_1 = 0.87, c_2 = 1.77, c_3 = 0.21, c_4 = 0.010, m = 6.0$	13.80%
C–F	$d_o = 0.0029, d_1 = 2.016, c = -1.33, d_2 = 1560, d_3 = 7e - 6, f = 5.6, k_s = 0.01$	20.86%
MSS	$(A = 740 \text{ MPa}, n = 0.153), \tau_s = 341.47 \text{ MPa}$	24.87%
C–L	$D_c = 0.0725$	290.2%
MMC[b]	$(A = 740 \text{ MPa}, n = 0.153), c_1 = 0.0432, c_2 = 326.3 \text{ MPa}, c_\theta^s = 0.9491$	14.69%
PMMS	$(A = 740 \text{ MPa}, n = 0.153), c_1 = 0.0633, c_2 = 329.3 \text{ MPa}, c_\theta^s = 0.9752$	14.55%

[a] Parameters in ( ) are determined from tests and NOT included in optimization process.
[b] The MMC model parameters are different from those in Ref. [6] because all 15 tests (rather than plane stress cases) are used in optimization in this paper.

process. The average error (the right hand side of Eq. (45)) can be used to evaluate the predictive capabilities of various models.

$$\underset{(c1,c2,\ldots)}{Min}(Error)_{av} = \underset{(c1,c2,\ldots)}{Min}\left[\frac{1}{N}\sum_{i=1}^{N}\left|\frac{\hat{\varepsilon}_f(\eta_i,\bar{\theta}_i) - \bar{\varepsilon}_{f,i}}{\bar{\varepsilon}_{f,i}}\right|\right] \tag{45}$$

The calibrated fracture loci can be plotted in the 3D space of stress triaxiality, Lode angle parameter and equivalent strain to fracture, which can give us a visualized overall view of the model prediction capabilities. Eight models selected to calibrate this material are shown in Figs. 3–10. The error of each individual test with respect to model prediction is indicated as an error bar in the 3D surface. The corresponding plane stress and plane strain conditions at each fracture locus are also drawn as a pink solid curve and a red dash line onto the 3D fracture surface.
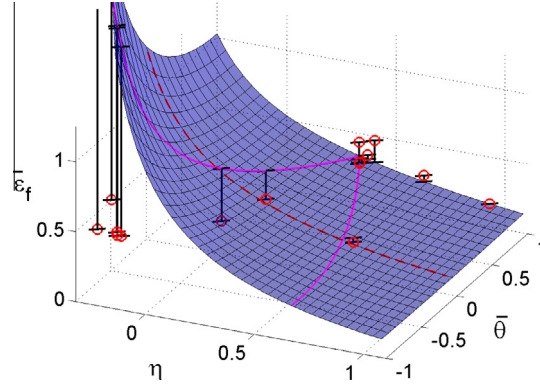
Fig. 3. Fracture locus of 2024-T351 Al alloy calibrated by McClintock model.
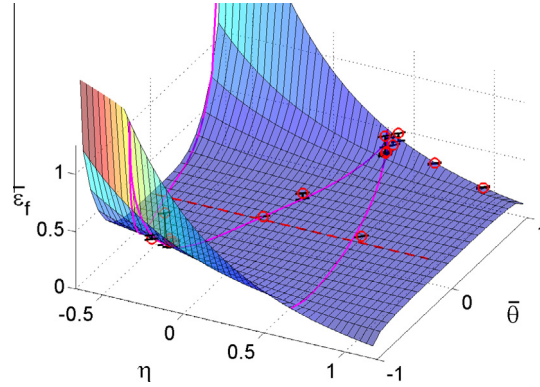
Fig. 4. Fracture locus of 2024-T351 Al alloy calibrated by Xue–Wierzbicki model.
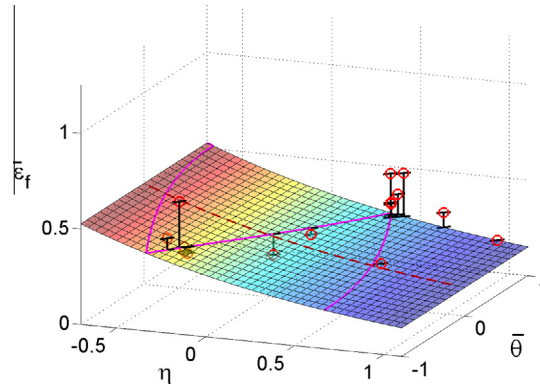
Fig. 5. Fracture locus of 2024-T351 Al alloy calibrated by Johnson–Cook model.
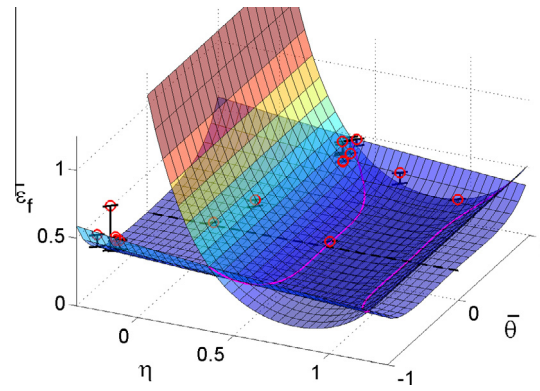
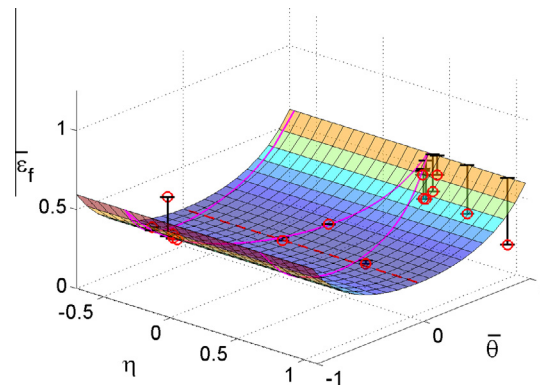**Fig. 6.** Fracture locus of 2024-T351 Al alloy calibrated by CrashFEM model.

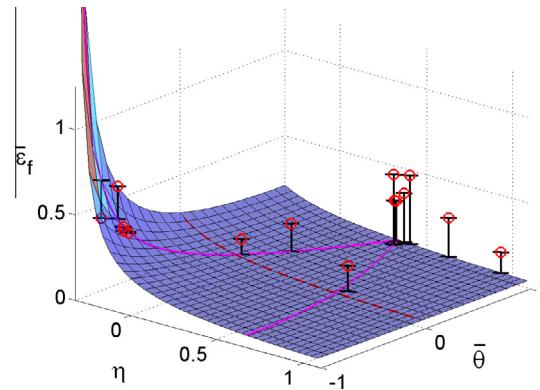**Fig. 7.** Fracture locus of 2024-T351 Al alloy calibrated by maximum shear stress criterion.

Fig. 8. Fracture locus of 2024-T351 Al alloy calibrated by Cockcroft–Latham model.

The McClintock's model is shown in Fig. 3. This model well predicts the decrease of material ductility as stress triaxiality increases at high stress triaxiality region, but it may fail to predict fracture at shear and compression where the stress tri-axiality is low or negative. Fig. 4 shows the result of Xue–Wierzbicki model, which is symmetric with respect to the Lode angle parameter. This model gives a good prediction of this set of 2024-T351 aluminum test data, but the exponential functions cannot satisfy the lower bound and upper bound assumptions for the whole range of stress triaxiality without special treatment. There is no cutoff value in the X–W model. The calibrated Johnson–Cook or Rice–Tracey model is illustrated in Fig. 5. The fracture locus of this model is independent of the Lode angle parameter. It well captures the effect of stress tri-axiality on fracture strains, but it does not consider the loss of ductility due to change of Lode angle parameter. Fig. 6 shows two fracture loci of the CrashFEM model. One is for ductile fracture and the other one is for shear fracture. The intersection
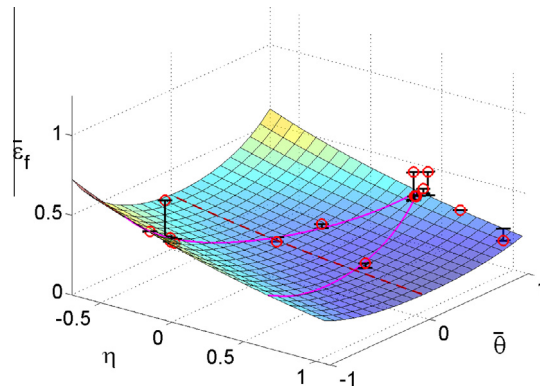
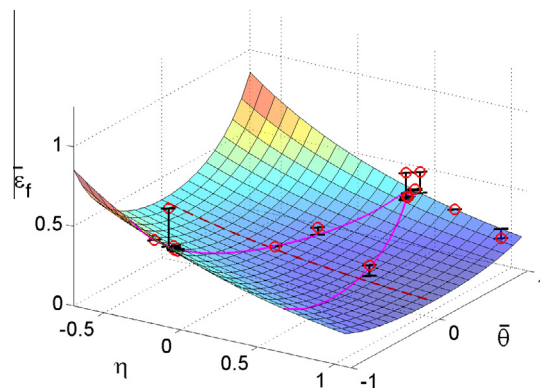**Fig. 9.** Fracture locus of 2024-T351 Al alloy calibrated by modified Mohr–Coulomb model.

Fig. 10. Fracture locus of 2024-T351 Al alloy calibrated by pressure modified maximum shear stress model.

curves of two loci are also plot. This model gives good prediction of given test data, but the validated region of stress triaxiality is from $-\frac{1}{3}$ to $\frac{2}{3}$ (the majority part of plane stress condition). The C-F model's prediction capability at high and low negative stress triaxiality regions needs further study.

Fig. 7 shows the fracture locus of the maximum shear stress criterion. Maximum shear stress is the main fracture mechanism of ductile fracture. This model performs well for 2024-T351 aluminum alloy because the ductility of this material is weakly dependent on stress triaxiality. The 3D representation of Cockcroft–Latham model is shown in Fig. 8. With only one fracture parameter, the model has similar prediction capability as that of McClintock's model. What's more, it can capture well fracture at the low stress triaxiality region around shear loading conditions. The model does not consider the loss of ductility due to Lode effect, so it cannot predict the non-monotonic trend of fracture strains at different loading conditions.

Fig. 9 presents the 3D fracture of modified Mohr–Coulomb criterion. The capability of this model is described in Ref. [6]. The dependency of fracture shear stress on normal stress gives similar exponential decay of material ductility with stress triaxiality. The effect of Lode angle parameter is also considered. A similar counterpart of MMC model is the pressure modified maximum shear stress model, that is plotted in Fig. 10. The fracture locus of PMMS is symmetric with respect to the Lode angle parameter, which is different from MMC asymmetric fracture locus. This model has similar prediction capabilities compared to the MMC model. Note that the Gurson type of models are not calibrated for this material due to lack of some physics based parameters.
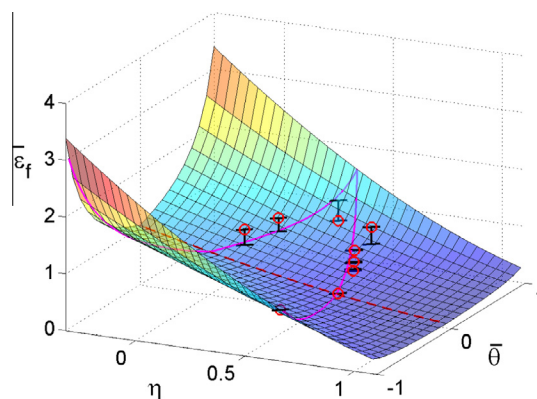
5. Model calibrations for TRIP780 steel sheet

The second material selected for calibration and comparison study is the TRIP780 steel sheet, which is one type of advanced high strength steel, extensively studied by Dunand and Mohr [19]. Optimizations of selected six fracture models' parameters were conducted based on the average stress state parameters (stress triaxiality and Lode angle parameter) reported in Table 1 of Ref. [19]. The same optimization objective (Eq. 45) was used. The Nielsen–Tvergaard type of Gurson model (N–T) was carefully calibrated by Dunand and Mohr [19] for this material. Some physics based parameters used in the comparison study were taken from this paper for Gurson type models. A list of calibrated model parameters is shown in Table 3. The 3D fracture loci of these six calibrated fracture models are illustrated in Figs. 11–16. Error of each individual test compared to model prediction is also marked onto the fracture surfaces.

Table 3
A list of calibrated model parameters for TRIP780 steel sheet.

Model	Parameters[a]	Average error (%)
C–L	$D_c = 0.6602$	25.80
WKS	$D_c = 2.4394, c_1 = 0.6837, \lambda = 1.6617, \mu = 1.6845$	15.20
MMC	$(A = 1460$ MPa$, n = 0.204), c_1 = 0.2945, c_2 = 952.38$ MPa$, c_0^s = 1.0192$	13.15
GNT	$(f_\circ = 6e-5), f_f = 0.05, (f_c = 0.067, f_N = 4.5e-2, q_1 = 1.0, q_2 = 0.7, \epsilon_N = 0.25, s_N = 0.1)$	27.77
GNH	$(f_\circ = 6e-5), f_f = 8.64e-5, (q_1 = 1.0, q_2 = 0.7), k_w = 0.2780$	17.00
N–T	$(f_\circ = 6e-5), f_f = 0.08, (f_c = 0.067, f_N = 4.5e-2, q_1 = 1.0, q_2 = 0.7), k_w = 2.4, (\epsilon_N = 0.25, s_N = 0.1, \eta_1 = 0.35, \eta_2 = 0.7);$	36.78

[a] Parameters in ( ) are determined from tests and NOT included in optimization process.
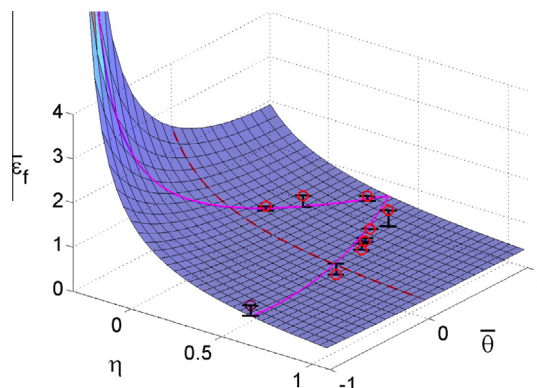
Fig. 11. Fracture locus of TRIP780 steel calibrated by Cockcroft–Latham model model.

Fig. 12. Fracture locus of TRIP780 steel calibrated by Wilkins model.

The Cockcroft–Latham model is calibrated again for the TRIP780 steel. As shown in Fig. 11, a much better correlation than 2024-T351 aluminum alloy is achieved for this material. Since this model has only one free parameter, it can provide a nice approximation when no sufficient test data is available. Fig. 12 shows the calibrated fracture locus of Wilkins' model. This model is very similar to the pressure modified maximum shear stress model (PMMS), which is also a symmetric fracture locus. Good prediction capability is found for the Wilkins' model. Fig. 13 shows the prediction from modified Mohr–Coulomb criterion (MMC). Good prediction capability of MMC model is also demonstrated for this material. The major difference between Wilkins and MMC fracture loci is at the extrapolated low and negative stress triaxiality regions. MMC model has a cutoff region, but Wilkins model does not. This part will be further compared in Section 7.

The fracture locus of the classical GNT Gurson model with only one parameter optimized (f_f) is illustrated in Fig. 14. This model shows monotonic decay of fracture strains as stress triaxiality increases. Since only the void growth mechanism under positive mean stress and the void nucleation mechanism are considered in this model, and void nucleation rate is usually very small, this model almost predicts no fracture at negative stress triaxiality region. The new void shear mechanism was introduced at the Nahshon-Hutchinson revision of Gurson model (GNH). The calibrated fracture locus with two parameters optimized (f_f and k_w) is shown in Fig. 15 as an example. Good prediction accuracy was obtained by GNH model
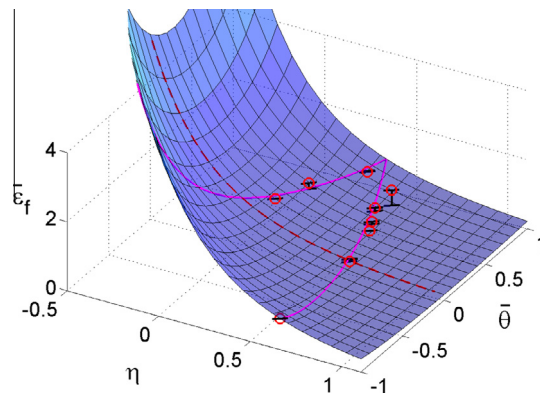
Fig. 13. Fracture locus of TRIP780 steel calibrated by modified Mohr–Coulomb model.
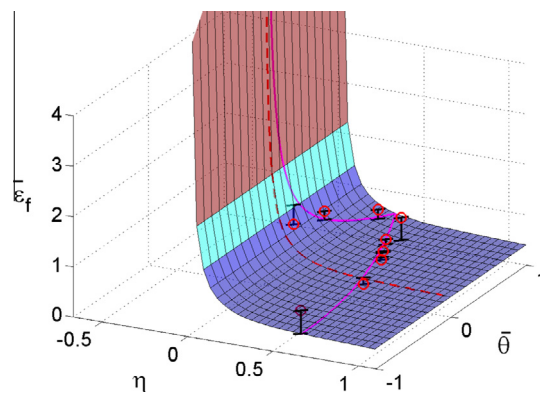

Fig. 14. Fracture locus of TRIP780 steel calibrated by GNT Gurson model.
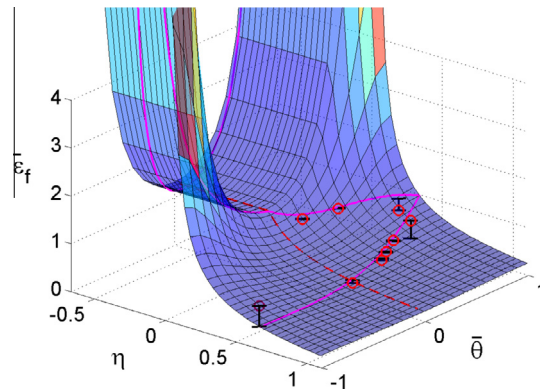

Fig. 15. Fracture locus of TRIP780 steel calibrated by Nahshon–Hutchinson Gurson model.

for the given test data. It is interesting to note that there is a non-smooth transition between negative and positive stress triaxiality regions. The reason is due to direct summation and uncoupling of two failure mechanisms (void growth and void shear). The further evolution of Gurson model is the Nielsen–Tvergaard one, which is plot in Fig. 16. Similar to the GNH model, this model well fits the given test data of TRIP780 steel sheet. One can see that there is a discontinuity of material ductility at zero stress triaxiality region. The main reason is due to the assumption that the total micro void volume fraction can be directly summed up for three different fracture mechanisms, see Eq. (17). Actually, the void shear will not increase the micro void volume fraction, which needs further research. More test data at negative stress triaxiality region are needed to fully evaluate this model.
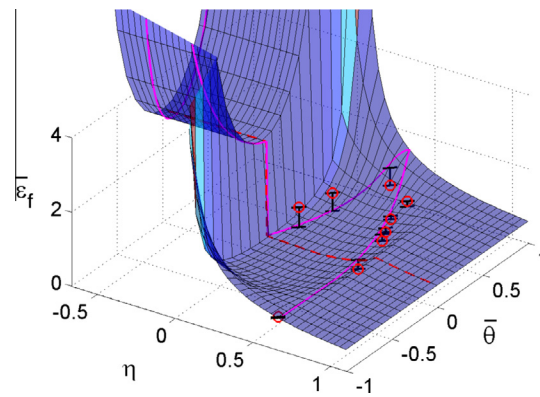
Fig. 16. Fracture locus of TRIP780 steel calibrated by Nielsen–Tvergaard Gurson model.

6. 2D representation for plane stress and plane strain fracture, $\hat{\varepsilon}_f(\eta)$

Plane stress and plane strain conditions are two common loading conditions in real applications. Plane stress condition is a widely used approximation for metal sheets, under which the stress triaxiality and Lode angle parameter are uniquely related by Eq. (3). Then, the stress triaxiality only can be used to distinguish different loading conditions. For generalized plane strain conditions, the Lode angle parameter is zero ($\bar{\theta} = 0$). Therefore, a 3D fracture locus can be simplified as 2D representation ($\hat{\varepsilon}_f(\eta)$) for both plane stress and plane strain conditions. Two types of advanced high strength steels (TRIP 780 and TRIP690) will be used in the 2D comparative study of various fracture models.

6.1. TRIP 780 steel

The TRIP 780 steel sheet has been calibrated for six fracture models in Section 5. Using the plane stress condition (Eq. (3)), the fracture loci can be presented in the 2D plane of equivalent strain to fracture and the stress triaxiality. The results of five models are shown in Fig. 17. The test data points are also plotted. One can see that both MMC and WKS models give good prediction accuracy in terms of overall trends. It is noted that the WKS model usually predicts much higher fracture strain at uni-axial tension than that of equal biaxial tension, which is not true in this material. Significant differences are observed for all five models at the extrapolated region at the negative stress triaxiality region. It should be mentioned that fracture test data at negative stress triaxiality regions are hard to get due to sheets buckling.

6.2. TRIP 690 steel

The third material reviewed in the paper is the TRIP690 steel sheets (also called RA-K40/70 provided by ThyssenKrupp Steel) reported by the presented authors [6]. Five different tests are conducted to calibrate this material's fracture properties all in plane stress, including uniaxial tension, notch tension, punch test, plane strain tension and simple shear tests. The
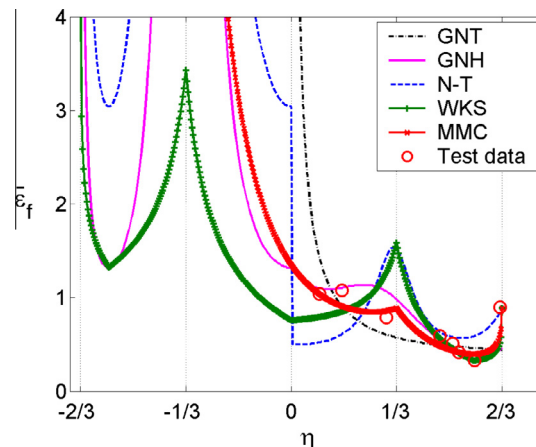

Fig. 17. Comparison of TRIP780 steel plane stress fracture in the 2D plane of equivalent strain to fracture and stress triaxiality for various models.

Table 4
A list of calibrated model parameters for TRIP690 steel sheet.

Model	Parameters[a]	Average error (%)
C–L	$D_c = 0.4397$	59.84
J–C	$c_0 = 0.1271, c_1 = 0.5161, c_2 = 0.7599$	21.97
MMC	$(A = 1275.9 \text{ MPa}, n = 0.2655), c_1 = 0.12, c_2 = 720 \text{ MPa}, c_\theta^s = 1.095$	15.38
GNH	$(f_0 = 6e-5), f_f = 8.7e-5, (q_1 = 1.0, q_2 = 0.5), k_w = 0.6$	23.00

[a] Parameters in ( ) are determined from tests and NOT included in optimization process.

stress state parameters and fracture strains for those tests are listed in Table 2 of Ref. [6]. Again, the average values of stress triaxiality and Lode angle parameter are used to compensate some parameter changes even under monotonic loading conditions. Four models are selected to calibrate this material, and the optimized model parameters are summarized in Table 4. Optical measurement with digital image correlation was used in those tests. The major strain and minor strain components at fracture initiation sites were measured and plotted in the Fracture Forming Limit Diagram (FFLD) plane, as illustrated in Fig. 18. The FFLD is an effective engineering tool to describe metal sheets fracture. The predictions of those four calibrated fracture models are also plotted in this figure for comparison. It is found that both MMC and GNH model show good prediction capability for the given test data. However, these two models predict significantly different fracture limits between uni-axial tension and shear loading conditions.

Among the five types of test data for TRIP690 steel sheets, two of them are under generalized plane strain condition ($\bar{\theta} = 0$): plane strain tension and simple shear. The predictions of plane strain fracture loci for these four fracture models are shown in Fig. 19. One can see all four models accurately predict the decay of fracture strains as stress triaxiality increases. However, significant differences are observed for all models at the extrapolated region of negative stress triaxiality.
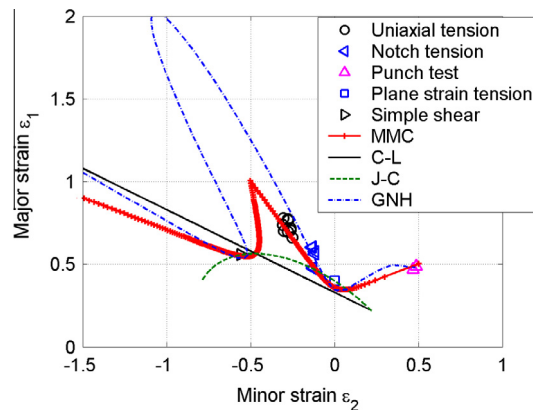
Fig. 18. Comparison of plane stress fracture in the fracture forming limit diagram for TRIP690 steel sheets.
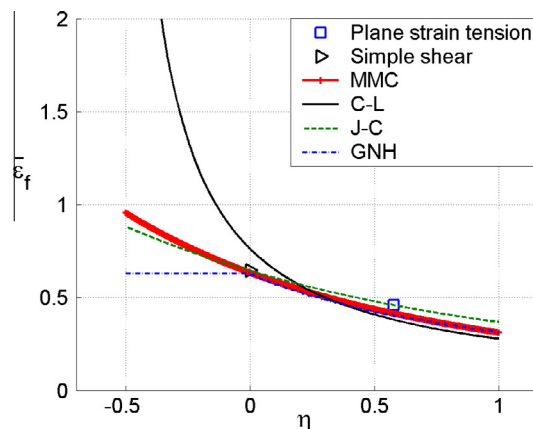
Fig. 19. Comparison of TRIP690 steel plane strain fracture in the 2D plane of equivalent strain to fracture and stress triaxiality for various models.

7. Existence of the cutoff region

The existence of cutoff value at the negative stress triaxiality region has been shown as an important feature for a ductile fracture locus [10,65,6]. Experimental study on the exact cutoff value/region is a big challenge due to limitations of current testing techniques. As discussed in Section 3, different ductile fracture models theoretically predict their own cutoff regions. A comparison of six models that exist cutoff region is shown in Fig. 20.

The Bao-Wierzbicki model indicates a cutoff value at $\eta = -\frac{1}{3}$ based on careful examination of the original Bridgman data [10]. This cut-off value is also explicitly incorporated to the fracture model by Lou et al. [48], Lou and Huh [47], and the value becomes changeable in their later revision [49]. The original Gurson model assumes no fracture at the negative stress triaxiality region. The McClintock and Crock-Latham models give almost the same cutoff region at the third branch of plane stress condition ($-\frac{2}{3} \leqslant \eta \leqslant -\frac{1}{3}$), because both models assume no fracture occurs under compressive dominated loadings (all principal stresses are not positive). It is also found that the McClintock cutoff region is very weakly dependent on hardening exponent n. The cutoff regions of the modified Mohr–Coulomb model (MMC) and pressure modified maximum shear stress model (PMMS) are dependent on the coefficient c_1. Both models predict a much lower value of cutoff region as the calibrated number. Two curves with an arbitrary value of $c_1 = 0.57$ are plotted in Fig. 20. The reason is probably due to the linear assumption of M–C and PMMS models in Eq. (26) and Eq. (30), which could not be suitable at very low negative stress triaxiality loading conditions. Further experimental investigation is needed to address this issue. The most recent research by Dunand [18] indicates that the relation between the shear and normal stress at the shear mode of failure is indeed nonlinear.

8. Differences of the second stress state parameter beside stress triaxiality

The stress triaxiality is already well accepted as a parameter to describe an arbitrary stress state, but stress triaxiality itself is not enough to fully distinguish different loading conditions. The second stress state parameter is needed. There are several parameters that can work for this purpose. In this section, comparison of these parameters will be made.

The stress triaxiality and equivalent stress are related to the first two stress invariants. The third deviatoric stress invariant (J_3) is a choice by nature. The normalized third deviatoric stress invariant ξ was used in Xue–Wierzbicki model [71,72], and the shear modified Gurson type models (GNH and N–T). The parameter A defined in Eq. (36) was used in Wilkins' model. The original Lode parameter was defined as the Eq. (46), which was used by Lou et al. [48]; Lou and Huh [47].

$$L = \frac{2\sigma_2 - \sigma_1 - \sigma_3}{\sigma_1 - \sigma_3} = \frac{2s_2 - s_1 - s_3}{s_1 - s_3} \tag{46}$$

A similar definition to the Lode parameter ($\chi = \frac{s_2 - s_3}{s_1 - s_3}$) was used by Xue [74] for fracture modeling. The normalized Lode angle (or called Lode angle parameter, $\bar{\theta}$) was used by the present authors [5,6]. Another similar parameter was proposed by Rudnicki and Rice [62] to describe a stress state, which is shown in Eq. (47). Although this parameter has not been used in fracture modeling, but comparison with others will help us better understand the physical meaning of the Lode angle.

$$N = \frac{s_2}{\tau} = \sqrt{3}\frac{s_2}{\sigma} \tag{47}$$

A comparison of these parameters for the full range of Lode angle parameter is shown in Fig. 21. One can see that the above parameters, except for A, are uniquely related and can serve as the second stress state parameter. There are approximate relationships among these parameters. For example, $L \approx -\bar{\theta}; L = 2\chi - 1; A \approx |\bar{\theta}|$ (WKS model); and $L = \sqrt{3}N$. Parameter selection is up to the convenience of a formulation.
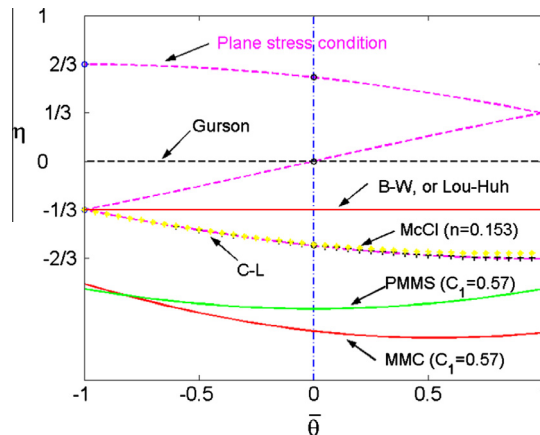

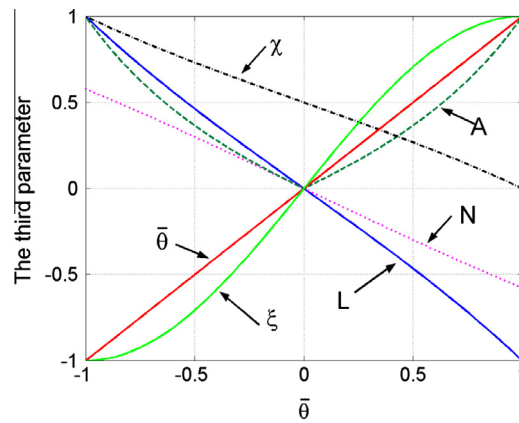**Fig. 20.** Comparison of cutoff regions of fracture loci on the stress state plane ($\eta, \bar{\theta}$).

Fig. 21. Comparison of different definitions of the second stress state parameter that can used in the ductile fracture modeling.

9. Conclusion and discussion

Several ductile fracture models, which are more related to the evaluation approach of this paper, are selected as examples and divided into three groups for a comparison study under the assumption of monotonic loading conditions. The first group is the physics based models, which include McClintock, Rice–Tracey, original Gurson and Gursion–Needlman–Tvergaard (GNT) models, and shear modified Gurson type models by Nahshon–Hutchinson and Nielsen–Tvergaard. The second group is phenomenological models, which include maximum shear stress model, Cockcroft–Latham criterion, pressure modified maximum shear stress, and modified Mohr–Coulomb criterion. The third group consists of empirical models, that includes Johnson–Cook, Bao–Wierzbicki, Xue–Wierzbicki, Wilkins, CrashFEM, and fracture forming limit diagram. A general stress state is described by two dimensionless parameters (the stress triaxiality and Lode angle parameter). Using the derived transformation equations for principal stresses and strain power hardening law assumptions, fracture loci of the above three groups of fracture models are expressed in the three dimensional space of equivalent strain to fracture, stress triaxiality and Lode angle parameter.

Optimization is set up to calibrate these three groups of fracture models for three sets of fracture data available in the literatures: TRIP 690 and TRIP 780 advanced high strength steel sheets and 2024-T351 aluminum alloy. The calibrated 3D fracture loci help to visualize the overall prediction capabilities of these models. A scalar measure of the error is introduced which can serve as one way of evaluating the accuracy of various fracture models, see Tables 2–4. It is noted that not all the models are calibrated for all three materials presented in the paper. The main reasons are due to lack of physics/test based parameters in some Gurson type models, and also due to limit the paper length. The similar calibration and optimization approaches can be applied to other materials by readers if interested.

The existence of cutoff region, which is a necessary feature of a ductile fracture model, is analyzed for each fracture model. Six of those models that have cutoff regions are compared and discussed. This comparison study gives a better understanding of merits of the existing ductile fracture models and provides some guidelines for usage of these models. There are many other published ductile fracture models that are not included in this paper, but the similar method can be used to study them.

It should be noted that all the above comparative studies are based on monotonic loading assumption. Some changes in the stress state parameters as specimens deform are compensated by the average values. Other optimization approaches can be found in Luo et al. [51]. In the cases of largely nonlinear strain paths, concepts of a damage (or the micro void fractions) accumulation rule should be invoked, which will make a direct comparison difficult. This part of research is ongoing and is not included in the present paper.

Acknowledgements

References

[1] Advanced high-strength steel applications design and stamping process guidelines – a special edition of in-depth advanced high-strength steel case studies. Technical report, Auto/Steel Partnership; 2010.
[2] Atkins AG, Mai YW. Elastic and plastic fracture. Chichester: Ellis Horwood; 1985.
[3] Bai Y. Fracture of 1045 steel under complex loading history. In: Proceedings of Numisheet 2011, Seoul, Korea, August 21–26; 2011.

[4] Bai Y, Wierzbicki T. Forming severity concept for predicting sheet necking under complex loading histories. Int J Mech Sci 2008;50(6):1012–22. http://dx.doi.org/10.1016/j.ijmecsci.2008.02.010. ISSN: 0020-7403. <http://www.sciencedirect.com/science/article/B6V49-4S0PKM4-1/2/c3512ef93882830e0c7886cab187b19e>.

[5] Bai Y, Wierzbicki T. A new model of metal plasticity and fracture with pressure and lode dependence. Int J Plast 2008;24(6):1071–96. http://dx.doi.org/10.1016/j.ijplas.2007.09.004. ISSN: 0749-6419. <http://www.sciencedirect.com/science/article/B6TWX-4PP2CSH-1/2/bfd7090c23e830cb987b428cffd186dc>.

[6] Bai Y, Wierzbicki T. Application of extended mohr-coulomb criterion to ductile fracture. Int J Fract 2010;161:1–20. http://dx.doi.org/10.1007/s10704-009-9422-8. ISSN: 0376-9429. <http://dx.doi.org/10.1007/s10704-009-9422-8>.

[7] Bao Y. Prediction of ductile crack formation in uncracked bodies. PhD thesis, Massachusetts Institute of Technology; 2003.

[8] Bao Y, Wierzbicki T. On fracture locus in the equivalent strain and stress triaxiality space. Int J Mech Sci 2004;46(1):81–98. <http://www.sciencedirect.com/science/article/B6V49-4BYR2P8-1/2/2c3ad89a1f17ea9e18fd57c7117c1cb1>.

[9] Bao Y, Wierzbicki T. A comparative study on various ductile crack formation criteria. J Engng Mater Technol 2004;126:314–24.

[10] Bao Y, Wierzbicki T. On the cut-off value of negative triaxiality for fracture. Engng Fract Mech 2005;72(7):1049–69. <http://www.sciencedirect.com/science/article/B6V2R-4DS6RB2-3/2/13abd4e661a040fd1f99880377331529>.

[11] Beissel SR, Holmquist TJ, Johnson GR. Influence of the third invariant in the ballistic impact of silicon carbide. Int J Impact Engng 2012;45(0):52–9. ISSN: 0734-743X. <http://www.sciencedirect.com/science/article/pii/S0734743X12000206>.

[12] Benzerga A, Surovik D, Keralavarma S. On the path-dependence of the fracture locus in ductile materials-analysis. Int J Plast 2012;37(0):157–70. ISSN: 0749-6419. doi: http://dx.doi.org/10.1016/j.ijplas.2012.05.003. <http://www.sciencedirect.com/science/article/pii/S0749641912000721>.

[13] Borvik T, Dey S, Clausen A. Perforation resistance of five different high-strength steel plates subjected to small-arms projectiles. Int J Impact Engng 2009;36(7):948–64. ISSN: 0734-743X. <http://www.sciencedirect.com/science/article/pii/S0734743X08003229>.

[14] Bridgman PW. Studies in large plastic flow and fracture. New York: McGraw-Hill; 1952.

[15] Bruenig M, Gerke S, Hagenbrock V. Micro-mechanical studies on the effect of the stress triaxiality and the lode parameter on ductile damage. Int J Plast 2013;50(0):49–65. ISSN: 0749-6419. doi: http://dx.doi.org/10.1016/j.ijplas.2013.03.012. <http://www.sciencedirect.com/science/article/pii/S074964191300082X>.

[16] Cockcroft MG, Latham DJ. Ductility and the workability of metals. J Inst Metals 1968;96:33–9.

[17] Coulomb C. Essai sur une application des regles des maximis et minimis a quelues problemes de statique relatifs al'architecture, Mem Acad Roy des Sci; 1776.

[18] Dunand M. Ductile fracture at intermediate stress triaxialities: experimental investigations and micro-mechanical modeling. PhD thesis, Massachusetts Institute of Technology; 2013.

[19] Dunand M, Mohr D. On the predictive capabilities of the shear modified gurson and the modified mohr-coulomb fracture models over a wide range of stress triaxialities and lode angles. J Mech Phys Solids 2011;59(7):1374–94. ISSN: 0022-5096. <http://www.sciencedirect.com/science/article/pii/S0022509611000688>.

[20] Gao X, Kim J. Modeling of ductile fracture: significance of void coalescence. Int J Solids Struct 2006;43:6277–93. <http://www.sciencedirect.com/science/article/B6VJS-4H74M97-2/2/3b24a669759db40d6453387bf6ce394a>.

[21] Gao X, Zhang T, Hayden M, Roe C. Effects of the stress state on plasticity and ductile failure of an aluminum 5083 alloy. Int J Plast 2009;25(12):2366–82. ISSN: 0749-6419. doi: http://dx.doi.org/10.1016/j.ijplas.2009.03.006. <http://www.sciencedirect.com/science/article/pii/S0749641909000485>.

[22] Goodwin G. Application of strain analysis to sheet metal forming in the press shop. In: SAE paper 680093; 1968.

[23] Griffith A. The phenomena of rupture and flow in solids. Philos Trans Roy Soc Lond Ser A 1921;221:163–98.

[24] Gudehus G. Elastoplastische stoffgleichungen fur trockenen sand. Ingenieur Archive 1973;42:151–69.

[25] Gurson A. Continuum theory of ductile rupture by void nucleation and growth, part i – Yield criteria and flow rules for porous ductile media. J Engng Mater Technol 1977;99:2–15.

[26] Gurson AL. Plastic flow and fracture behavior of ductile materials incorporating void nucleation, growth and interaction. PhD thesis, Brown University; 1975.

[27] Hancock JW, Brown DK. On the role of strain and stress state in ductile failure. J Mech Phys Solids 1983;31(1):1–24. <http://www.sciencedirect.com/science/article/B6TXB-46G2K1M-87/2/e6fcd075c309501a080e5fa7c8839559>.

[28] Hancock JW, Mackenzie AC. On the mechanisms of ductile failure in high-strength steels subjected to multi-axial stress-states. J Mech Phys Solids 1976;24(2–3):147–60. <http://www.sciencedirect.com/science/article/B6TXB-46G4XY9-15/2/659b0a9ca9dafdb5156b08e40c774f51>.

[29] Heath A, Gese H, Oberhofer G, Dell H. Modeling failure for nonlinear strain paths with crachfem. AIP Conf Proc 2013;1567(1):587–90. doi: http://dx.doi.org/10.1063/1.4850042. <http://scitation.aip.org/content/aip/proceeding/aipcp/10.1063/1.4850042>.

[30] Hooputra H, Gese H, Dell H, Werner H, Heath A. A new comprehensive failure model for crashworthiness simulation – validation for aluminum extrusions. In: 13th European conference on digital simulation for virtual prototyping, virtual manufacturing and virtual environment, Mainz, Germany; 2003.

[31] Hooputra H, Gese H, Dell H, Werner H. A comprehensive failure model for crashworthiness simulation of aluminium extrusions. Int J Crashworth 2004;9:449–64.

[32] Hosford W. A generalized isotropic yield criterion. J Appl Mech 1972;39:607.

[33] Irwin G. Analysis of stresses and strains near the end of a crack traversing a plate. J Appl Mech 1957;24:361–4.

[34] Johnson GR, Cook WH. Fracture characteristics of three metals subjected to various strains, strain rates, temperatures and pressures. Engng Fract Mech 1985;21(1):31–48. <http://www.sciencedirect.com/science/article/B6V2R-481DR3X-37/2/b7243b477f475eb0d2855ef21ac1e538>.

[35] Johnson GR, Holmquist TJ. Test data and computational strength and fracture model constants for 23 materials subjected to large strain, high strain rates, and high temperature, la-11463-ms. Technical report, Los Alamos National Laboratory; 1989.

[36] Kamoulakos A, Culiere P, Araki T. Prediction of ductile metal rupture with the e-w model in pam-crash. In: IBEC 2003 Chiba, Japan; 2003.

[37] Keeler S, Backhofen W. Plastic instability and fracture in sheet stretched over rigid punches. ASM Trans Quart 1964;56:25–48.

[38] Khan AS, Liu H. Strain rate and temperature dependent fracture criteria for isotropic and anisotropic metals. Int J Plast 2012;37(0):1–15. ISSN: 0749-6419. doi: http://dx.doi.org/10.1016/j.ijplas.2012.01.012. <http://www.sciencedirect.com/science/article/pii/S0749641912000137>.

[39] Khan AS, Liu H. A new approach for ductile fracture prediction on al 2024-t351 alloy. Int J Plast 2012;35(0):1–12. ISSN: 0749-6419. <http://www.sciencedirect.com/science/article/pii/S0749641912000046>.

[40] Le Roy G, Embury J, Edwards G, Ashby M. A model of ductile fracture based on the nucleation and growth of voids. Acta Metall 1981;29(8):1509–22. ISSN: 0001-6160. <http://www.sciencedirect.com/science/article/pii/0001616081901851>.

[41] Lecarme L, Tekoglu C, Pardoen T. Void growth and coalescence in ductile solids with stage {III} and stage {IV} strain hardening. Int J Plast 2011;27(8):1203–23. ISSN: 0749-6419. doi: http://dx.doi.org/10.1016/j.ijplas.2011.01.004. <http://www.sciencedirect.com/science/article/pii/S0749641911000052>.

[42] Lee Y-W. Fracture prediction in metal sheets. PhD thesis, Massachusetts Institute of Technology; 2005.

[43] Lemaitre J. A course on damage mechanics. Berlin, Germany: Springer; 1996.

[44] Li H, Fu M, Lu J, Yang H. Ductile fracture: experiments and computations. Int J Plast 2011;27(2):147–80. ISSN: 0749-6419. doi: http://dx.doi.org/10.1016/j.ijplas.2010.04.001. <http://www.sciencedirect.com/science/article/pii/S0749641910000598>.

[45] Li Y, Luo M, Gerlach J, Wierzbicki T. Prediction of shear-induced fracture in sheet metal forming. J Mater Process Technol 2010;210(14):1858–69. ISSN: 0924-0136. <http://www.sciencedirect.com/science/article/pii/S0924013610001925>.

[46] Lian J, Sharaf M, Archie F, Muenstermann S. A hybrid approach for modelling of plasticity and failure behaviour of advanced high-strength steel sheets. Int J Damage Mech 2012;22(2):188–218.
[47] Lou Y, Huh H. Extension of a shear-controlled ductile fracture model considering the stress triaxiality and the lode parameter. Int J Solids Struct 2013;50(2):447–55. ISSN: 0020-7683. doi: http://dx.doi.org/10.1016/j.ijsolstr.2012.10.007. <http://www.sciencedirect.com/science/article/pii/S002076831200426X>.
[48] Lou Y, Huh H, Lim S, Pack K. New ductile fracture criterion for prediction of fracture forming limit diagrams of sheet metals. Int J Solids Struct 2012;49(25):3605–15. ISSN: 0020-7683. <http://www.sciencedirect.com/science/article/pii/S002076831200056X>.
[49] Lou Y, Yoon JW, Huh H. Modeling of shear ductile fracture considering a changeable cut-off value for stress triaxiality. Int J Plast 2014;54(0):56–80. ISSN: 0749-6419. doi: http://dx.doi.org/10.1016/j.ijplas.2013.08.006. <http://www.sciencedirect.com/science/article/pii/S0749641913001617>.
[50] Luo M, Wierzbicki T. Numerical failure analysis of a stretch-bending test on dual-phase steel sheets using a phenomenological fracture model. Int J Solids Struct 2010;47(22–23):3084–102. http://dx.doi.org/10.1016/j.ijsolstr.2010.07.010. ISSN: 0020-7683. <http://www.sciencedirect.com/science/article/B6VJS-50KC6VT-1/2/67ad75f1a78d10b6db5f73df63a424b9>.
[51] Luo M, Dunand M, Mohr D. Experiments and modeling of anisotropic aluminum extrusions under multi-axial loading, Part ii: Ductile fracture. Int J Plast 2012;32–33(0):36–58. ISSN: 0749-6419. <http://www.sciencedirect.com/science/article/pii/S0749641911001896>.
[52] Malcher L, Pires FA, de Sa JC. An assessment of isotropic constitutive models for ductile fracture under high and low stress triaxiality. Int J Plast 2012;30–31(0):81–115. ISSN: 0749-6419. doi: http://dx.doi.org/10.1016/j.ijplas.2011.10.005. <http://www.sciencedirect.com/science/article/pii/S0749641911001690>.
[53] McClintock FA. A criterion of ductile fracture by the growth of holes. J Appl Mech 1968;35:363–71.
[54] Mohr D. Effect of stress-state on ductile fracture: experiments and modeling. In: International Symposium on Plasticity and Its Current Applications, Bahamas, January 3–8; 2013.
[55] Mohr O. Abhandlungen aus dem Gebiete der Technischen Mechanik. 2nd ed. Berlin: Ernst; 1914.
[56] Nahshon K, Hutchinson JW. Modification of the gurson model for shear failure. Eur J Mech A-Solid 2008;27(1):1–17.
[57] Needleman A, Tvergaard V. An analysis of ductile rupture in notched bars. J Mech Phys Solids 1984;32(6):461–90. <http://www.sciencedirect.com/science/article/B6TXB-46G2K9M-91/2/8745c3f1a46fb597913967f26e65753f>.
[58] Nielsen KL, Tvergaard V. Effect of a shear modified gurson model on damage development in a fsw tensile specimen. Int J Solids Struct 2009;46(3–4):587–601. ISSN: 0020-7683. <http://www.sciencedirect.com/science/article/pii/S0020768308003752>.
[59] Oh SI, Chen CC, Kobayashi S. Ductile fracture in axisymmetric extrusion and drawing—part 2: Workability in extrusion and drawing. J Engng Ind 1979;101(1):36–44. http://dx.doi.org/10.1115/1.3439471. <http://link.aip.org/link/?MSE/101/36/1>.
[60] Rice J. A path independent integral and the approximate analysis of strain concentration by notches and cracks. J Appl Mech 1968;35:379–86.
[61] Rice JR, Tracey DM. On the ductile enlargement of voids in triaxial stress fields. J Mech Phys Solids 1969;17:201–17.
[62] Rudnicki JW, Rice JR. Conditions for the localization of deformation in pressure-sensitive dilatant materials. J Mech Phys Solids 1975;23(6):371–94. <http://www.sciencedirect.com/science/article/B6TXB-46G50H8-K2/2/dad922897ef1963e604902f26b074797>.
[63] Stoughton TB, Yoon JW. A new approach for failure criterion for sheet metals. Int J Plast 2011;27(3):440–59. ISSN: 0749-6419. <http://www.sciencedirect.com/science/article/pii/S0749641910000951>.
[64] Tarigopula V, Hopperstad O, Langseth M, Clausen A, Hild F, Lademo O-G, et al. A study of large plastic deformations in dual phase steel using digital image correlation and fe analysis. Exp Mech 2008;48(2):181–96. http://dx.doi.org/10.1007/s11340-007-9066-4. ISSN: 0014-4851. doi: http://dx.doi.org/10.1007/s11340-007-9066-4.
[65] Teng X, Wierzbicki T. Evaluation of six fracture models in high velocity perforation. Engng Fract Mech 2006;73(12):1653–78. <http://www.sciencedirect.com/science/article/B6V2R-4JCBPDF-1/2/089b90721a40a1aae6f84883b5baf8b3>.
[66] Teng X, Wierzbicki T, Hiermaier S, Rohr I. Numerical prediction of fracture in the taylor test. Int J Solids Struct 2005;42(9–10):2929–48. ISSN: 0020-7683. <http://www.sciencedirect.com/science/article/pii/S0020768304005414>.
[67] Tresca H. Comptes Rendus Acad Sci 1864;59:754.
[68] Tvergaard V, Needleman A. Analysis of the cup-cone fracture in a round tensile bar. Acta Mater 1984;32:157–69.
[69] Voyiadjis GZ, Hoseini S, Farrahi G. Effects of stress invariants and reverse loading on ductile fracture initiation. Int J Solids Struct 2012;49(13):1541–56. ISSN: 0020-7683. doi: http://dx.doi.org/10.1016/j.ijsolstr.2012.02.030. <http://www.sciencedirect.com/science/article/pii/S0020768312000789>.
[70] Werner H, Hooputra H, Dell H, Gese H. A phenomenological failure model for sheet metals and extrusions. In: Annual review meeting and workshop of Impact and Crashworthiness Lab at MIT, Cambridge, MA; 2004.
[71] Wierzbicki T, Xue L. On the effect of the third invariant of the stress deviator on ductile fracture. Technical report, Impact and Crashworthiness Laboratory, Massachusetts Institute of Technology, Cambridge, MA; 2005.
[72] Wierzbicki T, Bao Y, Lee Y-W, Bai Y. Calibration and evaluation of seven fracture models. Int J Mech Sci 2005;47(4–5):719–43. <http://www.sciencedirect.com/science/article/B6V49-4G0M3XX-1/2/6ebd431547d5c5b1bdac30c7428bcffb>.
[73] Wilkins ML, Streit RD, Reaugh JE. Cumulative-strain-damage model of ductile fracture: simulation and prediction of engineering fracture tests, ucrl-53058. Technical report, Lawrence Livermore Laboratory, Livermore, California; 1980.
[74] Xue L. Damage accumulation and fracture initiation in uncracked ductile solids subject to triaxial loading. Int J Solids Struct 2007;44(16):5163–81. <http://www.sciencedirect.com/science/article/B6VJS-4MP56BV-1/2/30d3c7da24a040dc0faf92c5aad4b026>.
[75] Xue L. Constitutive modeling of void shearing effect in ductile fracture of porous materials. Engng Fract Mech 2008;75(11):3343–66. ISSN: 0013-7944. doi: http://dx.doi.org/10.1016/j.engfracmech.2007.07.022. <http://www.sciencedirect.com/science/article/pii/S0013794407003220>. Local Approach to Fracture (1986–2006): Selected papers from the 9th European Mechanics of Materials Conference.